

Mass Transport in Polymer Electrolyte Membrane Water Electrolyser Liquid-Gas Diffusion Layers: A Combined Neutron Imaging and X-ray Computed Tomography Study

M. Maier^a, J. Dodwell^a, R. Ziesche^a, C. Tan^{a,b}, T. Heenan^{a,b}, J. Majasan^a, N. Kardjilov^c, H. Markötter^c, I. Manke^c, L. Castanheira^d, G. Hinds^d, P.R. Shearing^{a,b}, D.J.L. Brett^{a,b,*}

^a *Electrochemical Innovation Lab, Department of Chemical Engineering, UCL, London, WC1E 7JE, United Kingdom*

^b *The Faraday Institution, Quad One, Harwell Science and Innovation Campus, Didcot, OX11 0RA, UK*

^c *Helmholtz-Zentrum Berlin (HZB), Hahn-Meitner-Platz 1, 14109 Berlin, Germany*

^d *National Physical Laboratory, Hampton Road, Teddington, Middlesex, TW11 0LW, UK*

* *Corresponding author. Tel.: +44 (0)20 7679 3310; fax: +44 (0)20 7383 2348. E-mail address: d.brett@ucl.ac.uk (D.J.L. Brett).*

Abstract

The increasing use of intermittent renewable energy sources calls for novel approaches to large-scale energy conversion and storage. Hydrogen can be readily stored and produced from renewable sources using polymer electrolyte membrane water electrolyzers (PEMWEs). Mass transport of water and product gas in the liquid-gas diffusion layer (LGDL) is critical for PEMWE performance, particularly at high current densities. In this work, neutron radiography is deployed to measure the spatial distribution of water within three different LGDLs, while X-ray micro-computed tomography (XCT) is used to characterize the microstructure of the LGDL materials. The combination of these two techniques yields valuable insight into water transport within the LGDL. Significant local water heterogeneity is observed and a link between flow-field geometry/location and LGDL mass transport is identified. It is further shown that the pore volume in these LGDLs is significantly under-utilized, pointing the way towards design optimisation of LGDL materials and architectures.

Keywords: PEM Water Electrolyser; Neutron Imaging; Mass Transport; X-ray Micro-Computed Tomography; Liquid-Gas Diffusion Layer; Two-phase Flow.

1 Introduction

The existence of a concentration (or mass transport) overpotential in polymer electrolyte membrane water electrolyzers (PEMWEs) is a major cause of performance limitation when operating at high current densities [1]. However, detailed mechanistic elucidation and reliable quantification of this effect is limited and tend to be empirical in nature [2–5]. The concentration overpotential primarily occurs at the anode at high current densities, when the generation of oxygen gas via the consumption of water exceeds the rate at which water can be supplied through flow channels and liquid-gas diffusion layers (LGDLs). Historically, the concentration overpotential was rarely of practical importance, as PEMWEs were not typically operated at high enough current densities to cause severe mass transport limitations. However, application-specific requirements require water electrolyzers to operate at higher current densities and technical improvements in the electrolyte and catalysts used are allowing the attainable power in PEMWEs to increase [6], and costs to fall [7,8], such that mass transport aspects are attracting more attention. Techniques that allow *operando* investigation of two-phase flow and water management are therefore of significant interest in the development of next-generation PEMWEs.

The ability of neutrons to penetrate many materials with a high molecular mass, while being strongly attenuated by specific light materials, such as hydrogen and lithium, has made neutron imaging a powerful tool for visualizing these elements in electrochemical energy conversion and storage devices [9]. Its use has been demonstrated for the imaging of Li-ion batteries, visualizing lithium migration and intercalation during charge and discharge [10]. The ability of neutron imaging to detect water and its concentration gradient in PEM fuel cells has been widely demonstrated [11–14], but there is limited literature on its use for investigating PEMWEs. Selamet et al. were the first to apply *operando* neutron imaging to a PEMWE. They used through-plane radiographs to quantify the water thickness in different regions of the active area and showed periodic growth and detachment of gas bubbles on the surface of the LGDL [15,16]. Hoeh et al. determined the water-to-gas ratio in a PEMWE at various current densities and water flow rates for land and channel areas in a PEMWE [17]. By deploying in-

plane neutron radiography, Seweryn et al. [18] discovered a counter-intuitive pattern of water distribution in the anode LGDL. They found the water content and gradient to be unaffected by current density in the range from 0.10 A cm^{-2} to 2.50 A cm^{-2} , which indicates a high water holdup in sintered titanium powder. Panchenko et al. [19] used in-plane neutron radiography to compare the mass transport characteristics of sintered titanium powder and titanium fibres as LGDLs. The authors found that the gas content of the sintered titanium powder (titanium sinter) varied more strongly with current density, indicating improved mass transport in the sintered powder LGDL. It was also found that the LGDL contained more gas under the land of the flow channels than under the channels. In a later study, the authors combined neutron imaging with high-speed optical imaging to investigate the role of water stoichiometry on mass transport in the flow channels and LGDLs [20]. Building on this previous work for neutron imaging of PEMWEs, Lee et al. [21] investigated the influence of nitrogen purging on the cathode side in order to find a set of ideal conditions for deploying neutron radiography for PEMWEs.

X-ray micro-computed tomography (XCT) has proven to be a valuable technique for the characterization of electrochemical devices. It is often applied to determine structural changes in Li-ion or related types of batteries [22–25] and has been successfully used to investigate water distribution in PEM fuel cells [26]. There are several publications demonstrating the use of XCT for investigating the microstructure of LGDL materials for PEMWEs. Zielke et al. [27] used XCT to examine different woven and sintered titanium samples and calculated electrical and thermal conductivities as well as water permeabilities based upon the microstructures of the samples. However, the authors did not provide any data on how these various LGDLs performed in a PEMWE. A similar study from Schuler et al. [28], obtained XCT data for a number of different titanium felts and a sinter material for comparison. It was found that the felts exhibited a significantly higher permeability and diffusivity, but a lower thermal conductivity than the sintered titanium. Majasan et al. [29,30] used XCT to investigate structural properties of sintered LGDLs with different particle sizes and combined XCT data with electrochemical characterization finding a link between microstructure and electrolyser performance.

This work uses operando through-plane neutron radiography of PEMWEs at average current densities of up to 1.50 A cm^{-2} to examine mass transport of water within LGDLs under rib (land) locations. Three different LGDL materials are investigated and XCT is employed to link the microstructure of the LGDL to its mass transport and water-gas holdup capacity.

2 Experimental

2.1 PEMWE Cell

The PEMWE cell used for these experiments (Figure 1), consisted of two aluminium end-plates, gold coated, aluminium parallel channel flow-field plates on both anode and cathode sides, a titanium LGDL on the anode side, Toray carbon paper as gas diffusion layer on the cathode side, and a catalyst coated membrane (CCM) with a square active area of 25 cm^2 . An aluminium holder was used at each end of the cell to ensure an even pressure distribution over the active area. The PEMWE cell was held together with four inner M3 screws (tightened to 1.7 Nm) and four outer M5 screws (tightened to 2.3 Nm). The flow-fields consisted of 15 parallel, vertical channels with a length of 5 cm, a depth of 3 mm, evenly distributed over the active area, which is similar to flow-field geometries previously employed [31–33].

Table 1: Description, thickness, and supplier of the three LGDLs used in this work. The ID will be used in the text to refer to a specific LGDL.

ID	Description	Thickness (mm)	Fibre Diameter (μm)	Supplier
Sinter	Sintered titanium particles	2.0	-	Merelex (USA)
Thick Felt	Sintered titanium fibres	1.0	20	NIKKO Techno (Japan)
Thin Felt	Sintered titanium fibres	0.1	20	NIKKO Techno (Japan)

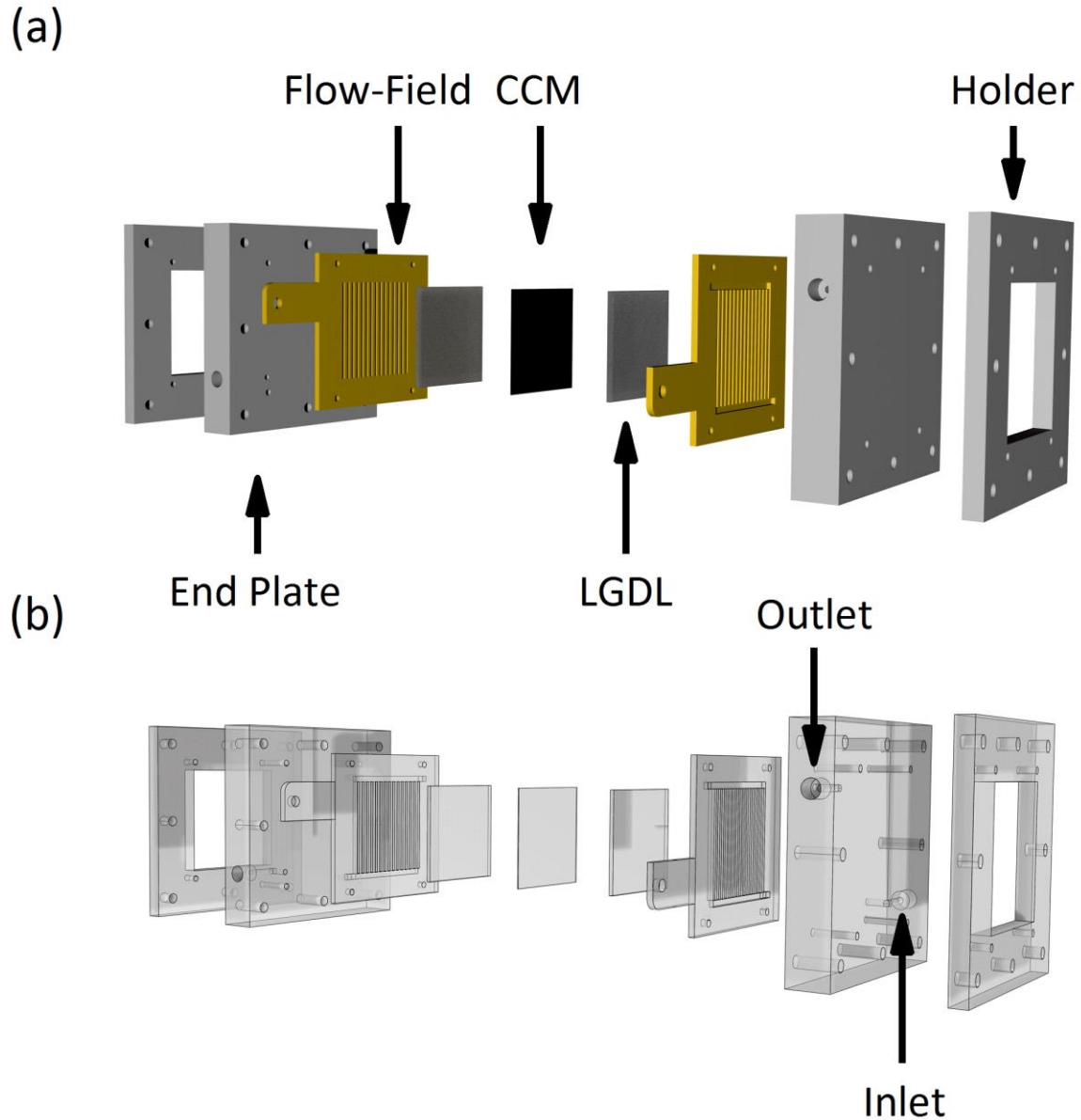


Fig. 1: PEMWE cell used for all experiments in this work. (a) The cell consists of two aluminium holders and end-plates, two gold-coated, aluminium, parallel channel flow-field plates, a titanium liquid-gas diffusion layer (LGDL) on the anode side, a carbon paper gas diffusion layer on the cathode side, and a catalyst coated membrane (CCM). (b) The water inlet is placed at the bottom of the flow-field, with the outlet being placed diagonally opposite at the top of the flow-field.

The CCM was based on Nafion 115, with 0.6 mg cm^{-2} of platinum on carbon on the cathode side and 3 mg cm^{-2} of iridium/ruthenium oxide on the anode side (ITM Power, UK). The different types of LGDL

are shown in Table 1. SEM Images of the LGDL materials can be found in Figure S1 in the Supplementary Information.

The parallel flow-fields were designed with diagonally opposing inlet and outlet, as described by Majasan et al. [34]. In these Z-type flow-fields a non-uniform distribution of water flow velocity and pressure is observed. Due to the pressure field enforced by the flow-field geometry, flow through the channels near the outlet is favoured. It was found that the flow velocity in the channels closest to the outlet is significantly higher than in the remainder of the channels (up to a factor of 5) [33,35,36].

Electrochemical testing was performed between 0.00 A cm^{-2} and 1.50 A cm^{-2} with an IviumStat potentiostat connected to an IviumBoost10012 (100 A, Ivium Technologies, Netherlands). Deionized water was circulated through the anode side of the PEMWE with an inflow temperature of $50 \text{ }^{\circ}\text{C}$ and a constant water flow rate of 100 ml min^{-1} , which equals a water ratio [31] of 47.6 at 1.50 A cm^{-2} . This high rate of water circulation was chosen to ensure effective gas removal in all channels such that the mass transport effects within the LGDL could be highlighted. The cathode side was run without water inflow. The electrochemical performance of the PEMWE cell is provided in Figure S2 in the Supplementary Information for all three LGDLs.

2.2 Neutron Imaging and Image Analysis

Neutron radiography was carried out at the Cold Neutron Tomography and Radiography beamline V7 (CONRAD) at Helmholtz-Zentrum Berlin, Germany. The beamline configuration has been described elsewhere [37,38]. The image acquisition and analysis process are visualized in Figure 2. For every set of conditions, 30 through-plane images were taken with an exposure time of 5 s. For the detector system [39] a pixel size of $23.9 \text{ }\mu\text{m}$ with a corresponding total field-of-view of $49 \times 49 \text{ mm}$ was set. Before starting an experiment with a specific LGDL, images without neutron beam (dark-field) and of the PEMWE cell before water was pumped through it (dry image) were taken (30 images each, 5 s exposure).

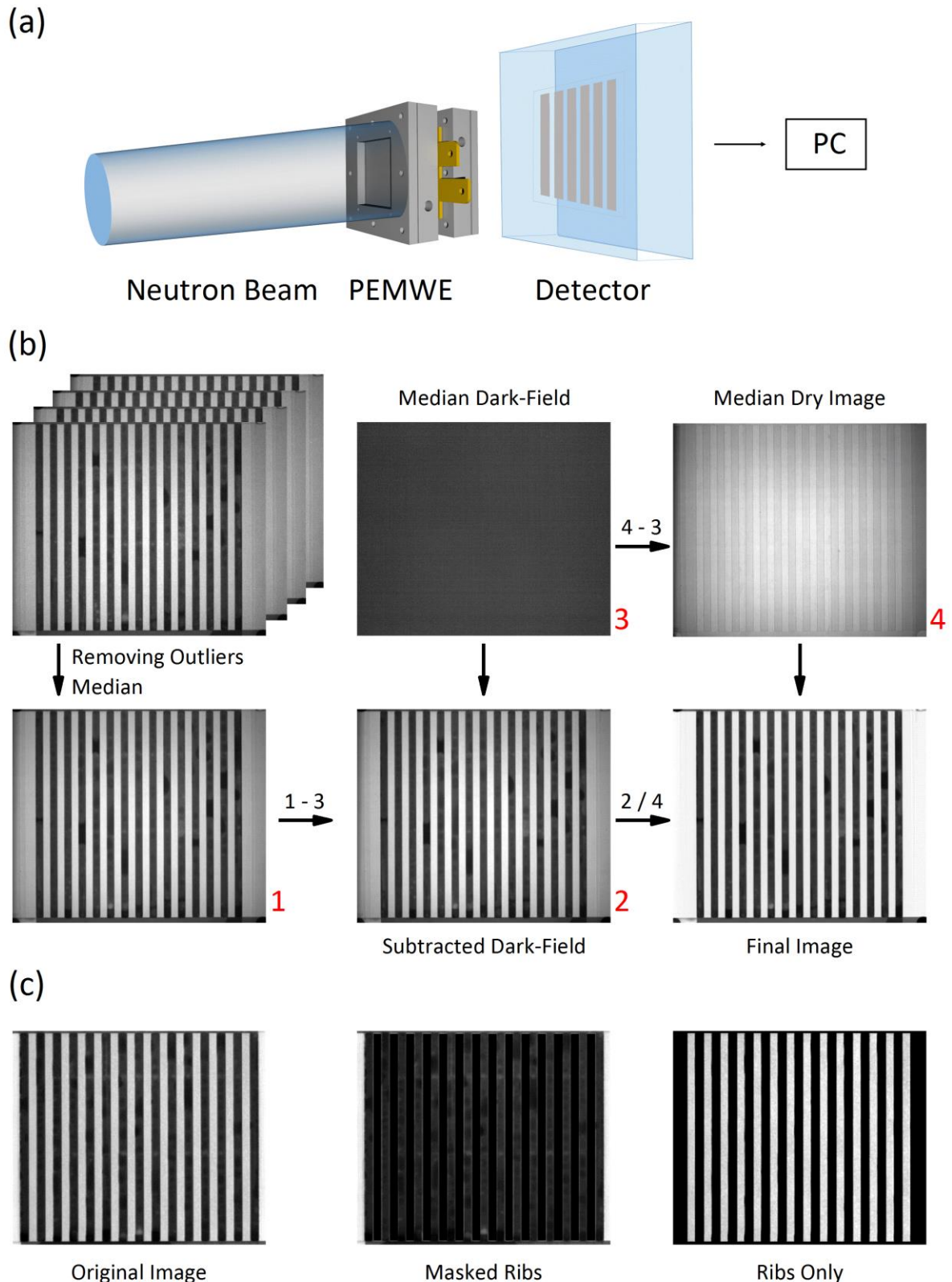


Fig. 2: (a) The PEMWE is placed in a neutron beam. Due to the material-dependent attenuation of the neutrons, a radiographic image of the PEMWE is captured by the detector. (b) Each set of 30 images is first filtered to remove outliers and averaged using a median. Then, the averaged dark-field is subtracted from the resulting image. This is then normalized with a dry image (also averaged) to obtain the final image. The greyscale values can be converted into the water thickness using the Beer-Lambert law. (c) The water thickness in the rib (land) areas is analysed separately by applying a mask, discarding the water thickness in the flow channels.

images (Radius: 2 pixels, Threshold: 50). Then each set of 30 images (PEMWE cell, dark-field, dry images) was median averaged to obtain a high signal-to-noise ratio. To account for the specific acquisition sensitivity of the CCD camera, the dark-field was subtracted from the averaged images of the PEMWE. These images were then normalized by dividing by the dry image. This accounts for dead pixels on the detector, the locally varying intensity of the neutron beam and also removes the contributions from PEMWE components which remain unchanged during operation (end-plates, flow-fields, and titanium in the LGDL). The greyscale value was converted to a water thickness using the Beer-Lambert law [11,19]. The distance between PEMWE cell and detector was 10 cm, which reduced the effect of neutron scattering and therefore improved the accuracy of the quantification of water thickness. For this distance between cell and detector, the attenuation coefficient of neutrons in water was 5.2 cm^{-1} , as provided by the beamline.

The purpose of this study is to examine the water/gas composition within the LGDL. To do this, the land locations are focused on as the open flow channels are dominated by relatively unstable two-phase flow with time-varying bubble dynamics, which precludes accurate analysis of the effective water thickness in the LGDL. Indeed, flow dynamics within channels have been extensively studied using optical cells [34,40–42], but it is the particular ability of neutron imaging to examine water under lands and within porous structures that is exploited here [17,19].

A potential limitation of the through-plane measurement technique is that the results for the water thickness are a summation of water through the anode, cathode and membrane components. This is another reason the water thickness is only quantified for the rib ('land') areas. As the CCM was fully hydrated before the experiments and remains so throughout these experiments, and the CCM and carbon paper are relatively thin, water in the LGDL of the anode side will dominate the neutron absorption response. However, it is expected that the water content in the carbon paper causes a decrease in accuracy in the measurement of water thickness.

2.3 X-ray Micro-Computed Tomography

X-ray computed tomograms were acquired for all LGDL materials used in this work. A Zeiss Xradia Versa 520 (Carl Zeiss X-ray Microscopy Inc., Pleasanton, CA) lab-based X-ray system was used to acquire the XCT datasets. The acquisition parameters are summarized in Table 2. Radiographic images were reconstructed into tomograms with the Zeiss Scout-and-Scan Control System Reconstructor software. Volume renderings were generated and analysed using Avizo (Thermo Fisher Scientific, US). The greyscale tomograms were then segmented using a manual threshold method according to the greyscale value. The porosity of the sample was calculated from this segmentation. Avizo was then used to create a pore network model (and the related pore size distribution), from which the flux of water at 50 °C through the LGDL with an input pressure of 1.3 bar and an output pressure at 1.0 bar was calculated in the software. Tortuosity values were calculated using TauFactor [43].

Table 2: Voltage, power, exposure time per projection, voxel size, and sample diameter chosen for acquisition over 360° of XCT datasets.

ID	Tube Voltage [kV]	Power [W]	Exposure Time [s]	Number of Projections	Voxel Size [μm]	Sample Diameter [mm]
Sinter	80	7	7	1601	1.85	3
Thick Felt	80	7	7	2401	1.52	3
Thin Felt	60	5	10	2401	1.52	3

2.4 Water Saturation and Residence Time

Information on the water saturation (fraction of pores filled with water) and the water residence time in the LGDL can be obtained by combining neutron imaging and XCT data. As mentioned in Section 2.2, the water thickness can only be reliably calculated for the rib areas. Hence, the analysis of water saturation and residence time is limited to these areas. The water saturation, S , is obtained by dividing the volume of water in the LGDL by the total pore volume. The water volume is the product of the averaged water thickness, D , and the active area, A . As the total pore volume of the LGDL is the product of its thickness, d , the porosity, ε , and the active area, one obtains:

$$S = \frac{D}{\varepsilon d} \quad (1)$$

This value indicates the fraction of pore volume that is filled with water, which equates to the pore utilization of the LGDL. Similarly, the average water residence time in the LGDL, τ , is obtained by dividing the amount of water in the LGDL by the total amount of water transported through it per unit time, M , which is comprised of the water consumption due to the oxygen evolution reaction (determined using Faraday's law and average current density) and electro-osmotic drag through the CCM. This assumes that all water entering the LGDL is either electrochemically reacted or carried across the membrane.

$$\tau = \frac{\rho DA}{M} \quad (2)$$

Details on the calculation of these mass flows were described by Ito et al. [31,44]. M is typically a gravimetric value, hence the density of water, ρ , is used to convert τ into a volumetric value.

3 Results

3.1 Structural Characterisation of LGDLs using X-ray CT

Tomograms of all three LGDL materials, as well as the pore size distribution (PSD), are shown in Figure

3. Values for the porosity (with and without disconnected pores), pore volume (product of LGDL volume and porosity), and the through-plane tortuosity are given in Table 3.

Table 3: Porosity, porosity without disconnected pores, pore volume, and through-plane tortuosity for the three LGDLs, obtained from XCT.

ID	Thickness [mm]	Porosity [%]	Porosity without disconnected pores [%]	Pore Volume [mm ³]	Tortuosity
Sinter	2.0	29.5	28.7	1476.4	3.3
Thick Felt	1.0	47.1	42.3	1177.3	2.2
Thin Felt	0.1	76.9	60.5	192.2	1.4

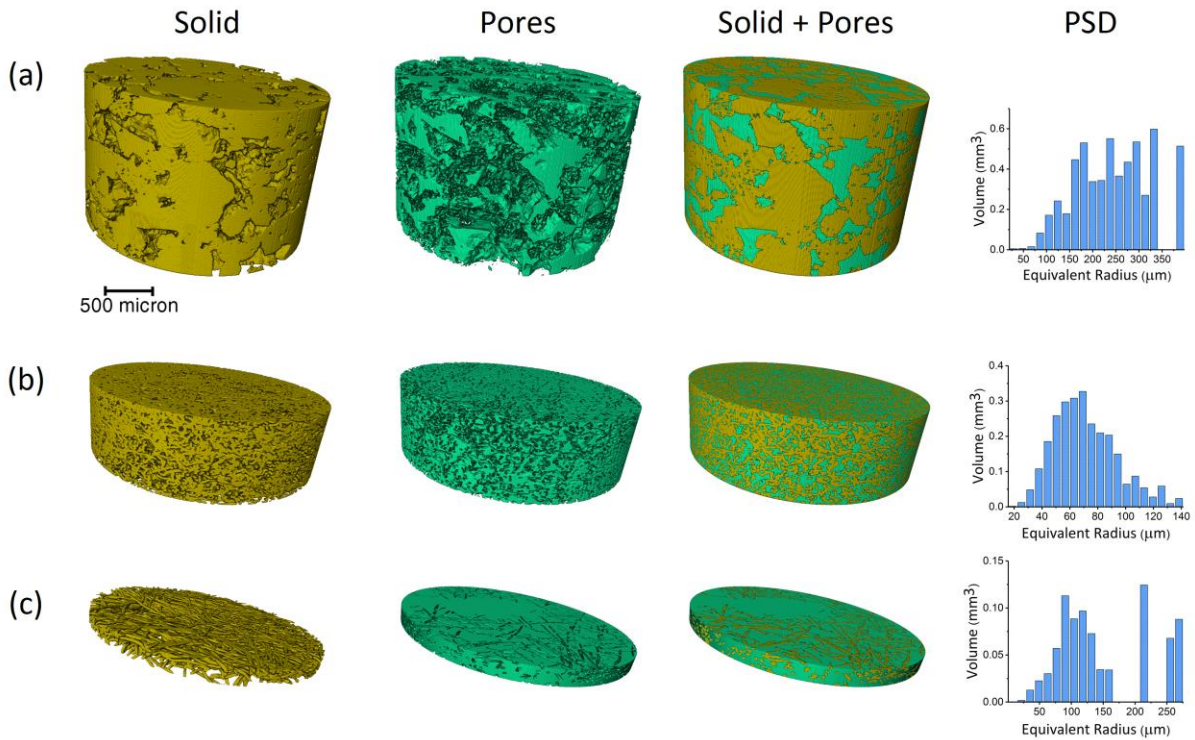


Fig. 3: X-ray micro computed tomograms of (a) sinter, (b) thick felt, and (c) thin felt. The solid material, pore space, conjunction of solid and pores, and the pore size distribution (PSD) are shown.

The sinter (Figure 3 (a)) exhibits a coarse structure of large particles with relatively few large pores. Porosity is found to be around 30 %, which is close to values previously found for sinter materials [45]. The vast majority of pore radii varied between 75 μm and 400 μm . A tortuosity of 3.3 was calculated for the sinter.

The thick felt (Figure 3 (b)) consists of densely packed titanium fibres, with fibres and pore space very evenly distributed. Porosity is around 47 %, significantly higher than for the sinter. The pore size distribution ranges from 20 μm to 140 μm , which is considerably smaller than for the sinter. The thick felt has a tortuosity of 2.2, which is 33 % lower than for the sinter.

While the sinter and the thick felt show mostly continuous PSDs, the thin felt exhibits a discontinuous distribution with pore volume being distributed among two main areas (Figure 3 (c)). A continuous distribution is observed between 25 μm and 160 μm , while significant pore volume is attributed to pores between 200 μm and 300 μm . Due to the low thickness, the thin felt effectively consists of a very small number of fibre layers, which means that many pores cover the whole thickness of the felt

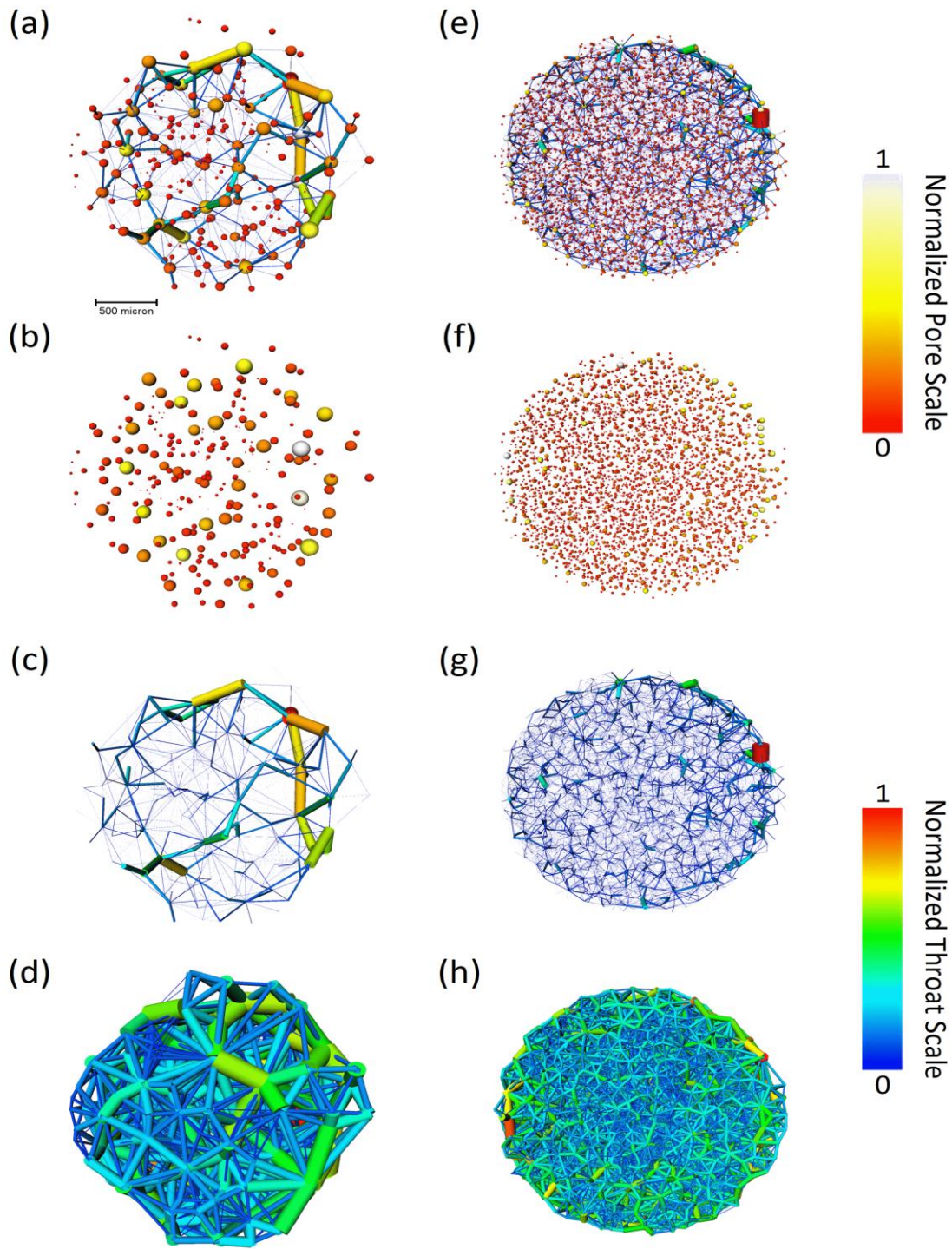


Fig. 4: Pore network model for the sinter ((a) – (d)) and the thick felt ((e) – (h)). The whole network ((a) and (e)) consists of pores (spheres) and throats (cylinders). Pores ((b) and (f)) are scaled according to their radius and colored according to their volume. Throats are scaled and colored by water flow through the respective throat ((c) and (g)), or according to their radius ((d) and (h)). The color maps are all normalized to the maximum value in the specific LGDL.

and are direct connections between the felt's top and bottom surface. Hence, the thickness of the thin

felt is not a limiting factor for the mass transport through its pores as water can flow directly through it to the surface of the catalyst layer. Due to its small thickness, the thin felt is also considerably less densely packed than the thick felt. Therefore, a high porosity of 77 % and a low tortuosity of 1.4 is obtained for the thin felt. As the thick felt is much more porous than the sinter, but only half as thick, these two LGDLs exhibit a similar pore volume of $\geq 1000 \text{ mm}^3$. The thin felt is much more porous than the sinter and thick felt, but due to its low thickness has a pore volume of only around 200 mm^3 . Hence it is expected that a much higher percentage of the thin felt is filled with water than for the other two LGDLs.

The differences in pore size and distribution are further illustrated in Figure 4, which shows the pore network model for the sinter and the thick felt. Due to the low thickness of the thin felt, no reliable pore network model could be created for this LGDL. The pore network model (Figure 4 (a) and (e)) consists of pores (spheres, Figure 4 (b) and (f)) and throats (cylinders, Figure 4 (c) and (g)). After calculating the flux of water through the pore network model (Section 2.3), the flow through each individual throat can be visualised (4 (c) and (g)). The same throat network is also displayed with the throats being scaled and colored by their radius (4 (d) and (h)). The comparison between the size-dependent and the flow-dependent scaling of the throats reveals that specific pathways for water flow through the LGDL are clearly favoured. The idea of preferential pathways through the LGDL of a PEMWE has been proposed and observed for oxygen gas bubbles [32] and for water transport [46,47] and is further supported by the negligible water flow through the majority of throats in the pore network model of sinter and thick felt. This indicates that a majority of flow occurs through a small fraction of available pathways, even though these pathways do not necessarily have wider throats.

3.2 Water Distribution using Neutron Imaging

Images of the active area of the PEMWE with LGDL and flow channels are shown as a function of current density for all three LGDLs in Figure 5, with the water thickness being displayed as a color map. For the LGDLs, a water thickness between 0.0 mm (white) and 0.5 mm (pink) is observed, while a water thickness between 0.6 mm (red) and 3.0 mm (black) is found in the flow channels. As current density

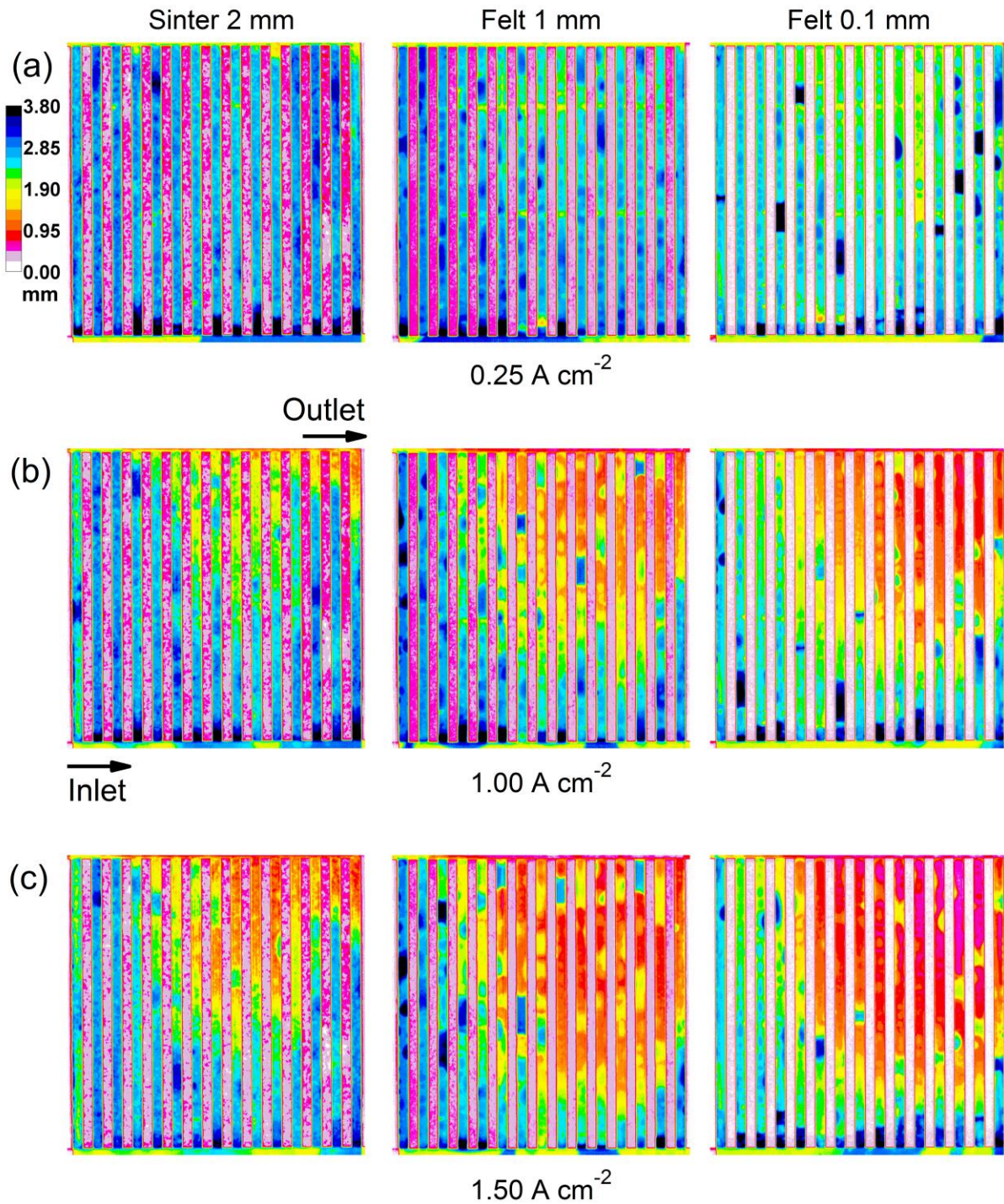


Fig. 5: Neutron radiographs at a current density of (a) 0.25 A cm⁻², (b) 1.00 A cm⁻², and (c) 1.50 A cm⁻² for all three LGDLs. The water thickness is displayed as a color map. The locations of the water inlet and outlet of the flow-field are indicated in (b) for the sinter.

is increased, the water thickness would be expected to decrease in the LGDL and the flow channels due to the higher water consumption rate (gas production rate). For the sinter, a clear trend of increasing amounts of oxygen (indicated by a reduction in water thickness) can be observed with

increasing current density. However, the decrease of water thickness is relatively modest over this range.

The same trend, albeit more pronounced, can be seen for both fibrous materials. The thin felt is already mostly filled with gas at a current density of 0.25 A cm^{-2} and exhibits a water thickness close to 0.0 mm for higher current densities across the whole active area. This illustrates the widely different gas and water transport properties of different materials due to their varying thicknesses and porosities. Furthermore, the porous structure of the sintered material with relatively larger pores can be clearly discerned, revealing its courser microstructure, as shown in Section 3.1. The felts, on the other hand, display a more homogenous distribution of gas, consistent with the smaller pore sizes found from the XCT analysis.

To quantify the water-gas transport characteristics of the LGDL materials, the water thickness over the rib (land) areas is examined in more detail (Figure 6). A mask is used, extracting only the pixel values of the individual rib areas, as described in Section 2.2. By analysing the average value over all 14 ribs (Figure 6 (a)), it is clear that all materials contain a decreasing amount of water with increasing current density. This is due to the increased water consumption, and the fact that water is increasingly displaced as more gas is produced at higher current densities. The thin felt retains much less water than the other two LGDLs due to its reduced thickness. On the other hand, the thick felt and the sinter contain almost identical amounts of water. As shown in Section 3.1, the thick felt is significantly more porous than the sinter, which facilitates a much higher water holdup for the thick felt, even with only half the thickness of the sinter.

At low current densities, the water thickness in the thin felt exceeds its physical thickness (0.1 mm), which is likely to be due to the contribution from the water content inside the carbon paper. In this case, the thicknesses of the CCM ($127 \mu\text{m}$) and carbon paper ($130 \mu\text{m}$) are comparable in magnitude to that of the thin felt and the water content of these introduces a significant measurement error. In

contrast, the thicknesses of the sinter and the thick felt far exceed that of CCM and carbon paper, and

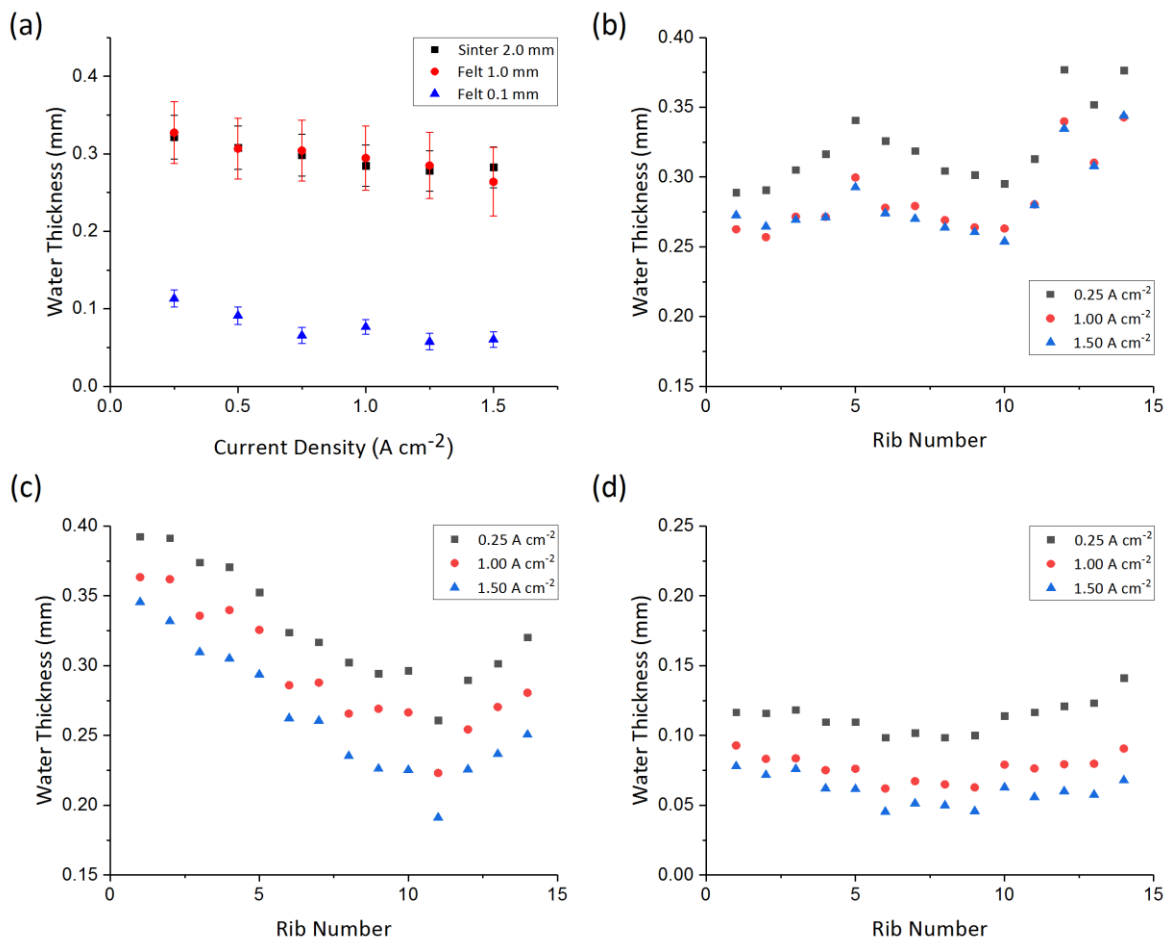


Fig. 6: (a) Water thickness in all three LGDLs as a function of current density. Spatially resolved water thickness over the rib area for the (b) sinter, (c) thick felt, and (d) thin felt at a current density of 0.25 A cm⁻², 1.00 A cm⁻², and 1.50 A cm⁻². Error bars indicate the standard deviation over the active area.

hence only a small relative uncertainty is introduced into the measurement for these two LGDLs. Furthermore, the overall trend of water thickness (spatially and with current density) is unaffected by this limitation of the measurement technique.

The water thickness in both the sinter and the thin felt reaches a plateau between 1.00 A cm⁻² and 1.25 A cm⁻² and does not decrease further. This might indicate that an equilibrium between water and gas transport has been reached, but experiments extending to higher current densities will be required to confirm this. Initially, when the current density is increased, new pathways through the LGDL are formed, which reduces the average water thickness of the LGDL. The formation of new gas

pathways and detachment sites from the surface of the LGDL have been observed by Hoeh et al. [32]. As the current density increases above a critical point, new pathways for gas removal can no longer be created, as all accessible pores are used either for gas removal or water transport. In this case, the mass transport rate through the LGDL can only be increased by accelerating the gas and water transport through existing pathways. This leads to an increase in gas bubble detachment frequency on the surface of the LGDL [32,48]. As no new pathways are formed, the ratio between water and gas transport pores remains constant, which causes the externally observable water thickness in the LGDL to remain constant (Figure 6 (a)).

When examining the difference in water thickness between individual ribs for the three LGDLs (Figures 6 (b)-(d)), clear differences are visible. All three materials show a decrease of water thickness with increasing current density across all ribs. The sinter (Figure 6 (b)) shows little local variance over the first 10 ribs, but a continuous increase in water thickness for the last four ribs. The thick felt (Figure 6 (c)) exhibits a clear gradient in water thickness, but also an increase in water thickness for the last four ribs.

This can potentially be explained by the uneven water flow velocity distribution in the parallel flow-field. As mentioned earlier (Section 2.1) the flow-field in this work is of the Z-flow pattern, which favors flow through the channels on the far right side (closer to the outlet) [33,35,36]. The water velocity in the final channel is up to five times higher than in the middle channels and this coincides with an increase of water thickness for the sinter and the thick felt in the same area. This implies that the heterogeneity in water flow distribution affects the LGDL and leads to higher measured water thickness. The results therefore indicate a close link between the water velocity in the flow channels and the water content and mass transport in the LGDL under the land.

Interestingly, the thin felt (Figure 6 (d)) shows almost no local gradient in water thickness. This indicates that the thin felt has a very limited capacity for water and gas, likely due to its small thickness,

high porosity, and low tortuosity. Hence the constant flow of water over the surface of the thin felt exposed to the flow channels is sufficient to enforce a very uniform water-gas distribution.

3.3 LGDL Water Content and Residence Time

Water content (saturation) and residence time as a function of current density, averaged over the entire active area, were calculated according to Section 2.4 and are displayed for the sinter and the thick felt in Figure 7. Due to the comparable thickness with the water-saturated CCM, the calculated values for the thin felt exhibited large standard deviation and are omitted from the analysis.

For the sinter, average water saturation (Figure 7 (a)) ranges from 54 % at 0.25 A cm^{-2} to 47 % at 1.50 A cm^{-2} . Similar values are found for the thick felt; however, the water saturation is slightly higher than for the sinter due to the lower pore volume of the thick felt. Around half of the pore volume of the LGDLs is not used for water transport within the range of current density in this work. The water residence time (Figure 7 (b)) varies between 42 s and 6 s for the sinter, and between 68 s and 8 s for the thick felt.

The linear extrapolation in Figure 7 (a) indicates the water saturation at 0.00 A cm^{-2} , which is 56.0 % and 70.6 % for the sinter and felt, respectively. This illustrates that a significant fraction of the LGDL is not filled with water, even without gas being produced due to electrochemical activity. The XCT analysis in Section 3.1 showed that a fraction of the LGDL pores are disconnected and can therefore not contribute to the transport of gas and water. However, for the sinter and thick felt there was only a moderate amount of disconnected porosity, which is not significant enough to explain the low values of water saturation obtained, even at 0.00 A cm^{-2} . This leads to the conclusion that a number of pores, which are connected to the rest of the pore network, are not, or insufficiently, reached by water flow (stranded pores). This effect has been computationally predicted for fibrous materials used in redox flow batteries and is affiliated with small variations in local porosity [49].

Based on this characterization, it seems likely that the performance of a PEMWE could be further improved by tailoring the LGDL to avoid disconnected or stranded ('dead') pore space. This could be

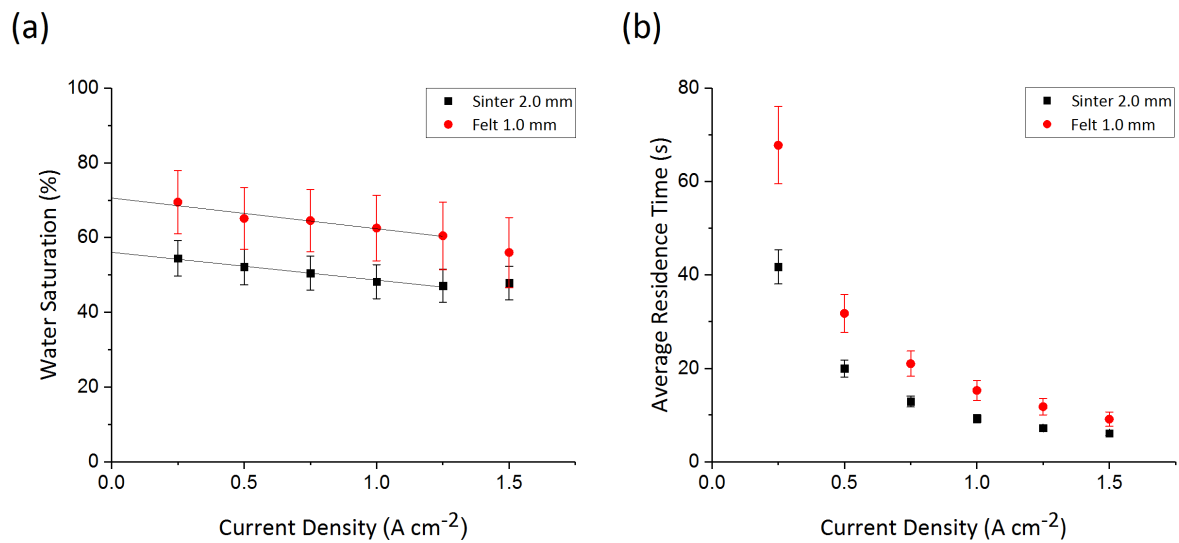


Fig. 7: (a) Water saturation and (b) average water residence time in the LGDL for the sinter and thick felt between 0.00 A cm⁻² and 1.50 A cm⁻² at a constant water flow rate of 100 ml min⁻¹. Error bars indicate the standard deviation over the active area.

achieved by reducing pore volume, which increases electrical and thermal conductivity but does not affect the mass transport properties of the LGDL. Another potential approach is to create materials in which the formation of new water pathways is favored, so that sufficient mass transport can be guaranteed even at elevated current density. The approach of combining neutron radiography and XCT is a promising technique for the evaluation of new materials and LDGL architectures.

4 Conclusion

This work combines X-ray micro-computed tomography and neutron radiography to investigate the link between LGDL microstructure and mass transport properties. Three different LGDLs were examined (one sintered and two fibrous materials); the sinter was found to have a porosity of ~30%, while the thick and thin felt have porosities of 47% and 77%, respectively. Pore network models were created from the XCT datasets and used to calculate the flux of water through individual throats of

the LGDL. It was found that the flow occurs predominantly through a small fraction of throats, supporting the idea of preferential pathways through the LGDL.

Neutron radiography was employed for *operando* imaging of a PEMWE, varying the LGDL material. Various differences between the three LGDLs were observed during operation of the PEMWE, with water thickness being clearly influenced by thickness and porosity of the LGDL.

To further investigate the differences between LGDL materials, the water thickness under the rib areas of the flow-fields was analysed. This offers the potential to observe the spatially-resolved water content in the LGDL only.

The main findings from this analysis are:

- A decrease in water thickness with increasing current density was revealed for all LGDLs, which is caused by the increased rate of gas production. Even though the materials exhibit strongly different microstructures, the gradient of water thickness with increasing current density is comparable for all three LGDLs.
- Significant inhomogeneity in water thickness was observed for the sinter and the thick felt across the active area. This highlights the need for novel LGDL structures or materials to avoid poor performance due to local mass transport limitations at high current density.
- Increased water thickness was found in areas that are likely to exhibit increased flow velocity in the flow channels. This indicates a link between flow-field geometry and mass transport in the LGDL, which has not been previously reported in literature. This is likely to be caused by an increase of gas removal and water supply to the respective areas of the LGDL.

By combining water thickness data obtained by neutron radiography and microstructural information gained from XCT, water saturation and water residence time in the pores of the LGDLs were calculated. It was revealed that a major fraction of the pore volume is not utilized for water transport and that this value varies only by about 10 % with increasing current density. Furthermore, the water residence

time in the LGDL was measured to range between 6 s and 68 s. Extrapolation to 0.00 A cm^{-2} shows that a significant fraction of pores remains dry even in the absence of electrochemical activity. This cannot be explained from the amount of disconnected pores found in the XCT analysis and therefore implies the existence of stranded pores. These pores are connected to the overall pore network, but no water flow through them occurs due to small scale variations in porosity in the vicinity of these pores. This indicates that further improvements on LGDL structure and materials need to be made to increase pore utilization. The reduction of unused pore volume can potentially lead to an improved usage of active area and hence to an improvement in the efficiency of PEMWEs.

The above findings illustrate the powerful capabilities of neutron imaging as a diagnostic tool for PEMWEs. The combination of neutron radiography and XCT yields deep insight into the mass transport characteristics of LGDLs, which would not be possible by either of these techniques alone. The findings give an indication of the shortcomings of the materials most frequently used as LGDLs in PEMWEs and suggest pathways to novel structures that could mitigate these issues. Future research directions will use this combination of diagnostic techniques to investigate the influence of different flow-field geometries on water management in the LGDL.

Acknowledgements

The authors acknowledge financial support into the EIL's hydrogen and fuel cell activity from the EPSRC through grants (EP/R023581/1; EP/P009050/1; EP/N032888/1; EP/M014371/1; EP/M009394; EP/L015749/1; EP/K038656/1). Support from the UK National Measurement System is also gratefully acknowledged. We thank HZB for the allocation of neutron radiation beamtime and all the excellent support. MM would like to thank the STFC Batteries Network for financial support (ST/R006873/1).

References

- [1] M. Carmo, D.L. Fritz, J. Mergel, D. Stolten, A comprehensive review on PEM water electrolysis, *Int. J. Hydrogen Energy*. 38 (2013) 4901–4934. doi:10.1016/j.ijhydene.2013.01.151.
- [2] Z. Kang, J. Mo, G. Yang, Y. Li, D.A. Talley, B. Han, F.Y. Zhang, Performance Modeling and

- Current Mapping of Proton Exchange Membrane Electrolyzer Cells with Novel Thin/Tunable Liquid/Gas Diffusion Layers, *Electrochim. Acta.* 255 (2017) 405–416. doi:10.1016/j.electacta.2017.09.170.
- [3] B. Han, J. Mo, Z. Kang, F.Y. Zhang, Effects of membrane electrode assembly properties on two-phase transport and performance in proton exchange membrane electrolyzer cells, *Electrochim. Acta.* 188 (2016) 317–326. doi:10.1016/j.electacta.2015.11.139.
- [4] Z. Abdin, C.J. Webb, E.M. Gray, Modelling and simulation of a proton exchange membrane (PEM) electrolyser cell, *Int. J. Hydrogen Energy.* 40 (2015) 13243–13257. doi:10.1016/j.ijhydene.2015.07.129.
- [5] R. García-Valverde, N. Espinosa, A. Urbina, Simple PEM water electrolyser model and experimental validation, *Int. J. Hydrogen Energy.* 37 (2012) 1927–1938. doi:10.1016/j.ijhydene.2011.09.027.
- [6] A. Buttler, H. Spliethoff, Current status of water electrolysis for energy storage, grid balancing and sector coupling via power-to-gas and power-to-liquids: A review, *Renew. Sustain. Energy Rev.* 82 (2018) 2440–2454. doi:10.1016/j.rser.2017.09.003.
- [7] O. Schmidt, A. Gambhir, I. Staffell, A. Hawkes, J. Nelson, S. Few, Future cost and performance of water electrolysis: An expert elicitation study, *Int. J. Hydrogen Energy.* 42 (2017) 30470–30492. doi:10.1016/j.ijhydene.2017.10.045.
- [8] S.M. Saba, M. Müller, M. Robinius, D. Stolten, The investment costs of electrolysis – A comparison of cost studies from the past 30 years, *Int. J. Hydrogen Energy.* 43 (2018) 1209–1223. doi:10.1016/j.ijhydene.2017.11.115.
- [9] N. Kardjilov, I. Manke, R. Woracek, A. Hilger, J. Banhart, Advances in neutron imaging, *Mater. Today.* 21 (2018) 652–672. doi:10.1016/j.mattod.2018.03.001.
- [10] J.B. Siegel, X. Lin, A.G. Stefanopoulou, D.S. Hussey, D.L. Jacobson, D. Gorsich, Neutron Imaging of Lithium Concentration in LFP Pouch Cell Battery, *J. Electrochem. Soc.* 158 (2011) A523. doi:10.1149/1.3566341.
- [11] R.J. Bellows, M.Y. Lin, M. Arif, A.K. Thompson, D. Jacobson, Neutron Imaging Technique for In Situ Measurement of Water Transport Gradients within Nafion in Polymer Electrolyte Fuel Cells, *J. Electrochem. Soc.* 146 (1999) 1099–1103.
- [12] R. Satija, D.L. Jacobson, M. Arif, S.A. Werner, In situ neutron imaging technique for evaluation of water management systems in operating PEM fuel cells, *J. Power Sources.* 129 (2004) 238–245. doi:10.1016/j.jpowsour.2003.11.068.
- [13] I.A. Schneider, S. Von Dahlen, M.H. Bayer, P. Boillat, M. Hildebrandt, E.H. Lehmann, P. Oberholzer, G.G. Scherer, A. Wokaun, Local transients of flooding and current in channel and land areas of a polymer electrolyte fuel cell, *J. Phys. Chem. C.* 114 (2010) 11998–12002. doi:10.1021/jp102259q.
- [14] P. Boillat, D. Kramer, B.C. Seyfang, G. Frei, E. Lehmann, G.G. Scherer, A. Wokaun, Y. Ichikawa, Y. Tasaki, K. Shinohara, In situ observation of the water distribution across a PEFC using high resolution neutron radiography, *Electrochem. Commun.* 10 (2008) 546–550. doi:10.1016/j.elecom.2008.01.018.
- [15] O.F. Selamet, U. Pasaogullari, D. Spornjak, D.S. Hussey, D.L. Jacobsen, M.D. Mat, In-situ two-phase flow investigation of Proton Exchange Membrane (PEM) electrolyzer by simultaneous optical and neutron imaging, *ECS Trans.* 41 (2011) 349–362.
- [16] O.F. Selamet, U. Pasaogullari, D. Spornjak, D.S. Hussey, D.L. Jacobson, M.D. Mat, Two-phase flow in a proton exchange membrane electrolyzer visualized in situ by simultaneous neutron

- radiography and optical imaging, *Int. J. Hydrogen Energy*. 38 (2013) 5823–5835. doi:10.1016/j.ijhydene.2013.02.087.
- [17] M.A. Hoeh, T. Arlt, N. Kardjilov, I. Manke, J. Banhart, D.L. Fritz, J. Ehlert, W. Lüke, W. Lehnert, In-operando Neutron Radiography Studies of Polymer Electrolyte Membrane Water Electrolyzers, *ECS Trans.* 69 (2015) 1135–1140.
- [18] J. Seweryn, J. Biesdorf, T.J. Schmidt, P. Boillat, Communication—Neutron Radiography of the Water/Gas Distribution in the Porous Layers of an Operating Electrolyser, *J. Electrochem. Soc.* 163 (2016) F3009–F3011. doi:10.1149/2.0641607jes.
- [19] O. Panchenko, E. Borgardt, W. Zwaygardt, F.J. Hackemüller, M. Bram, N. Kardjilov, T. Arlt, I. Manke, M. Müller, D. Stolten, W. Lehnert, In-situ two-phase flow investigation of different porous transport layer for a polymer electrolyte membrane (PEM) electrolyzer with neutron spectroscopy, *J. Power Sources*. 390 (2018) 108–115. doi:10.1016/j.jpowsour.2018.04.044.
- [20] O. Panchenko, L. Giesenberg, E. Borgardt, W. Zwaygardt, N. Kardjilov, H. Markötter, T. Arlt, I. Manke, M. Müller, D. Stolten, W. Lehnert, Influence of Stoichiometry on the Two-Phase Flow Behavior of Proton Exchange Membrane Electrolyzers, *Energies*. 12 (2019) 350. doi:10.3390/en12030350.
- [21] C.H. Lee, R. Banerjee, N. Ge, J.K. Lee, B. Zhao, E. Baltic, J.M. LaManna, D.S. Hussey, D.L. Jacobson, R. Abouatallah, R. Wang, A. Bazylak, The effect of cathode nitrogen purging on cell performance and in operando neutron imaging of a polymer electrolyte membrane electrolyzer, *Electrochim. Acta*. 279 (2018) 91–98. doi:10.1016/j.electacta.2018.05.066.
- [22] O.O. Taiwo, T.M.M. Heenan, D.P. Finegan, D.J.L. Brett, P.R. Shearing, J.M. Paz-García, S.A. Hall, R. Mokso, P. Villanueva-Pérez, A. Patera, Microstructural degradation of silicon electrodes during lithiation observed via operando X-ray tomographic imaging, *J. Power Sources*. 342 (2017) 904–912. doi:10.1016/j.jpowsour.2016.12.070.
- [23] D.P. Finegan, E. Darcy, M. Keyser, B. Tjaden, T.M.M. Heenan, R. Jervis, J.J. Bailey, R. Malik, N.T. Vo, O. V. Magdysyuk, R. Atwood, M. Drakopoulos, M. DiMichiel, A. Rack, G. Hinds, D.J.L. Brett, P.R. Shearing, Characterising thermal runaway within lithium-ion cells by inducing and monitoring internal short circuits, *Energy Environ. Sci.* 10 (2017) 1377–1388. doi:10.1039/c7ee00385d.
- [24] D.P. Finegan, M. Scheel, J.B. Robinson, B. Tjaden, I. Hunt, T.J. Mason, J. Millichamp, M. Di Michiel, G.J. Offer, G. Hinds, D.J.L. Brett, P.R. Shearing, In-operando high-speed tomography of lithium-ion batteries during thermal runaway, *Nat. Commun.* 6 (2015) 23. doi:10.1038/ncomms7924.
- [25] C. Tan, T.M. M Heenan, R.F. Ziesche, S.R. Daemi, J. Hack, M. Maier, S. Marathe, C. Rau, D.J. L Brett, P.R. Shearing, Four-Dimensional Studies of Morphology Evolution in Lithium–Sulfur Batteries, *Cite This ACS Appl. Energy Mater.* XXXX. 1 (2018) 5090–5100. doi:10.1021/acsaem.8b01148.
- [26] P. Krueger, H. Markoetter, J. Haußmann, M. Klages, T. Arlt, J. Banhart, C. Hartnig, I. Manke, J. Scholta, Synchrotron X-ray tomography for investigations of water distribution in polymer electrolyte membrane fuel cells, *J. Power Sources*. 196 (2011) 5250–5255. doi:10.1016/j.jpowsour.2010.09.042.
- [27] L. Zielke, A. Fallisch, N. Paust, R. Zengerle, S. Thiele, Tomography based screening of flow field / current collector combinations for PEM water electrolysis, *RSC Adv.* 4 (2014) 58888–58894. doi:10.1039/C4RA12402B.
- [28] T. Schuler, R. De Bruycker, T.J. Schmidt, F.N. Büchi, Polymer Electrolyte Water Electrolysis: Correlating Porous Transport Layer Structural Properties and Performance: Part I.

- Tomographic Analysis of Morphology and Topology, *J. Electrochem. Soc.* 166 (2019) F270–F281. doi:10.1149/2.0561904jes.
- [29] J.O. Majasan, F. Iacoviello, J.I.S. Cho, M. Maier, X. Lu, T.P. Neville, I. Dedigama, P.R. Shearing, D.J.L. Brett, Correlative study of microstructure and performance for porous transport layers in polymer electrolyte membrane water electrolyzers by X-ray computed tomography and electrochemical characterization, *Int. J. Hydrogen Energy.* (2019). doi:10.1016/j.ijhydene.2019.05.222.
- [30] J.O. Majasan, F. Iacoviello, P.R. Shearing, D.J. Brett, Effect of Microstructure of Porous Transport Layer on Performance in Polymer Electrolyte Membrane Water Electrolyser, *Energy Procedia.* 151 (2018) 111–119. doi:10.1016/j.egypro.2018.09.035.
- [31] H. Ito, T. Maeda, A. Nakano, Y. Hasegawa, N. Yokoi, C.M. Hwang, M. Ishida, A. Kato, T. Yoshida, Effect of flow regime of circulating water on a proton exchange membrane electrolyzer, *Int. J. Hydrogen Energy.* 35 (2010) 9550–9560. doi:10.1016/j.ijhydene.2010.06.103.
- [32] M.A. Hoeh, T. Arlt, I. Manke, J. Banhart, D.L. Fritz, W. Maier, W. Lehnert, In operando synchrotron X-ray radiography studies of polymer electrolyte membrane water electrolyzers, *Electrochem. Commun.* 55 (2015) 55–59. doi:10.1016/j.elecom.2015.03.009.
- [33] J. Nie, Y. Chen, S. Cohen, B.D. Carter, R.F. Boehm, Numerical and experimental study of three-dimensional fluid flow in the bipolar plate of a PEM electrolysis cell, *Int. J. Therm. Sci.* 48 (2009) 1914–1922. doi:10.1016/j.ijthermalsci.2009.02.017.
- [34] J.O. Majasan, J.I.S. Cho, I. Dedigama, D. Tsaoulidis, P. Shearing, D.J.L. Brett, Two-phase flow behaviour and performance of polymer electrolyte membrane electrolyzers: Electrochemical and optical characterisation, *Int. J. Hydrogen Energy.* 43 (2018) 15659–15672. doi:10.1016/j.ijhydene.2018.07.003.
- [35] J. Wang, H. Wang, Discrete approach for flow field designs of parallel channel configurations in fuel cells, *Int. J. Hydrogen Energy.* 37 (2012) 10881–10897. doi:10.1016/j.ijhydene.2012.04.034.
- [36] J. Wang, H. Wang, Flow-field designs of bipolar plates in PEM fuel cells: Theory and applications, *Fuel Cells.* 12 (2012) 989–1003. doi:10.1002/fuce.201200074.
- [37] N. Kardjilov, A. Hilger, I. Manke, CONRAD-2: Cold Neutron Tomography and Radiography at BER II (V7), *J. Large-Scale Res. Facil. JLSRF.* 2 (2016) 2–7. doi:10.17815/jlsrf-2-108.
- [38] N. Kardjilov, A. Hilger, I. Manke, R. Woracek, J. Banhart, CONRAD-2: The new neutron imaging instrument at the Helmholtz-Zentrum Berlin, *J. Appl. Crystallogr.* 49 (2016) 195–202. doi:10.1107/S1600576715023353.
- [39] S.H. Williams, A. Hilger, N. Kardjilov, I. Manke, M. Strobl, P.A. Douissard, T. Martin, H. Riesemeier, J. Banhart, Detection system for microimaging with neutrons, *J. Instrum.* 7 (2012). doi:10.1088/1748-0221/7/02/P02014.
- [40] I. Dedigama, P. Angeli, K. Ayers, J.B. Robinson, P.R. Shearing, D. Tsaoulidis, D.J.L. Brett, In situ diagnostic techniques for characterisation of polymer electrolyte membrane water electrolyzers - Flow visualisation and electrochemical impedance spectroscopy, *Int. J. Hydrogen Energy.* 39 (2014) 4468–4482. doi:10.1016/j.ijhydene.2014.01.026.
- [41] I. Dedigama, P. Angeli, N. Van Dijk, J. Millichamp, D. Tsaoulidis, P.R. Shearing, D.J.L. Brett, Current density mapping and optical flow visualisation of a polymer electrolyte membrane water electrolyser, *J. Power Sources.* 265 (2014) 97–103. doi:10.1016/j.jpowsour.2014.04.120.

- [42] M. Maier, Q. Meyer, J. Majasan, C. Tan, I. Dedigama, J. Robinson, J. Dodwell, Y. Wu, L. Castanheira, G. Hinds, P.R. Shearing, D.J.L. Brett, Operando flow regime diagnosis using acoustic emission in a polymer electrolyte membrane water electrolyser, *J. Power Sources*. 424 (2019) 138–149. doi:10.1016/j.jpowsour.2019.03.061.
- [43] S.J. Cooper, A. Bertei, P.R. Shearing, J.A. Kilner, N.P. Brandon, TauFactor: An open-source application for calculating tortuosity factors from tomographic data, *SoftwareX*. 5 (2016) 203–210. doi:10.1016/j.softx.2016.09.002.
- [44] H. Ito, T. Maeda, A. Nakano, C.M. Hwang, M. Ishida, A. Kato, T. Yoshida, Experimental study on porous current collectors of PEM electrolyzers, *Int. J. Hydrogen Energy*. 37 (2012) 7418–7428. doi:10.1016/j.ijhydene.2012.01.095.
- [45] S.A. Grigoriev, P. Millet, S.A. Volobuev, V.N. Fateev, Optimization of porous current collectors for PEM water electrolyzers, *Int. J. Hydrogen Energy*. 34 (2009) 4968–4973. doi:10.1016/j.ijhydene.2008.11.056.
- [46] C.H. Lee, J. Hinebaugh, R. Banerjee, S. Chevalier, R. Abouatallah, R. Wang, A. Bazylak, Influence of limiting throat and flow regime on oxygen bubble saturation of polymer electrolyte membrane electrolyzer porous transport layers, *Int. J. Hydrogen Energy*. 42 (2017) 2724–2735. doi:10.1016/j.ijhydene.2016.09.114.
- [47] F. Arbabi, A. Kalantarian, R. Abouatallah, R. Wang, J.S. Wallace, A. Bazylak, Feasibility study of using microfluidic platforms for visualizing bubble flows in electrolyzer gas diffusion layers, *J. Power Sources*. 258 (2014) 142–149. doi:10.1016/j.jpowsour.2014.02.042.
- [48] E. Leonard, A.D. Shum, S. Normile, D.C. Sabarirajan, D.G. Yared, X. Xiao, I. V Zenyuk, Operando X-ray tomography and sub-second radiography for characterizing transport in polymer electrolyte membrane electrolyzer, *Electrochim. Acta*. 276 (2018) 424–433. doi:10.1016/j.electacta.2018.04.144.
- [49] M.D.R. Kok, R. Jervis, D. Brett, P.R. Shearing, J.T. Gostick, Insights into the Effect of Structural Heterogeneity in Carbonized Electrospun Fibrous Mats for Flow Battery Electrodes by X-Ray Tomography, *Small*. 14 (2018) 1–15. doi:10.1002/sml.201703616.